Movements of Mycoplasma mobile Gliding Machinery Detected by High-Speed Atomic Force Microscopy

Movements of Mycoplasma mobile Gliding Machinery Detected by High-Speed Atomic Force Microscopy

Kohei Kobayashi, Noriyuki Kodera, Taishi Kasai, Yuhei O. Tahara, Takuma Toyonaga, Masaki Mizutani, Ikuko Fujiwara, Toshio Ando, Makoto Miyata

Citation	mBio. 12(3); e00040-21
Issue Date	2021-06-29
Published	2021-05-28
Type	Journal Article
Textversion	Publisher
Highlights	◆最小細胞である「マイコプラズマ・モービレ」の分子モーターの動きを世界で初めて検出。 ◆マイコプラズマの滑走運動時の動きを捉えた世界初の研究。 ◆ナノスケールのデバイスや医薬品を開発するための基礎となる。
概要	研究チームは、最小の細菌である「マイコプラズマ・モービレ」が滑走するための分子モーターの動きを検出することに世界で初めて成功しました。この発見は、ナノスケールのデバイスや医薬品の開発への応用が期待されます。 【今回の発見】 マイコプラズマは、菌体の片側に小さな突起“接着器官”を形成し、この突起で宿主組織の表面にはりつき、はりついたまま“滑走運動”を行います。滑走運動時には ATP 合成酵素から進化した特殊な分子モーターが細胞内部で力を発生していることが示唆されていましたが、その動きが捉えられたことはありませんでした。今回、最先端技術である高速原子間力顕微鏡（高速 AFM）を用いることで、滑走の分子モーターの動きをナノレベルで細胞外から検出することに成功しました。
Rights	© 2021 Kobayashi et al. This is an open-access article distributed under the terms of the Creative Commons Attribution 4.0 International license. https://creativecommons.org/licenses/by/4.0/
DOI	10.1128/mBio.00040-21

Description

<研究の内容>

本研究では、マイコプラズマを生きたままガラスに固定し、高速 AFM の細い針で細胞の表面を軽くたたきながら探ることにより、分子モーターの構造をリアルタイムにビデオに記録しました。

さらに得られたビデオ画像に隠された信号を計算によって抽出することで、分子モーター粒子が ATP を加水分解して力を発生する際の動きをナノレベルで追跡することに成功しました。その結果、鎖状に連なったモーター粒子が、細胞進行方向に向かって右側に約 9 ナノメートル、細胞内側に 2 ナノメートル、300 ミリ秒以内の時間に動くことを明らかにしました。このことは、他に類を見ない構造であるマイコプラズマの分子モーターがどのようなメカニズムで滑走運動を行っているか、そしてそのメカニズムが ATP 合成酵素のどのような性質から進化してきたかを説き明かす大きな手掛かりとなります。

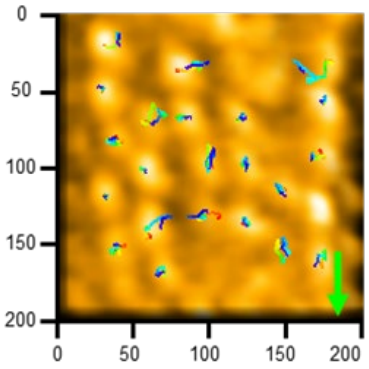

可視化された細胞内部のモーター粒子とその動き

縦方向に並ぶ白い楕円がモーター粒子。

緑の矢印は滑走運動の方向を示す。

それぞれの粒子の重心の 5 秒間の動きが虹色の線で示されている。

©大阪市立大学　宮田真人

<今後の展開>

ガラスに固定した細胞から膜を除去したり、単離した分子モーターを使ったりすることにより、空間的、時間的により高い分解能における解析を目指します。それとは別に単離した分子モーター構造を電子顕微鏡で解析することで、原子レベルの解像度で明らかにします。これらの情報を統合することで、滑走運動メカニズムを原子レベルで理解します。

滑走の構造とメカニズムを詳細に明らかにすることで、運動能の起源と動作原理に迫ることができ、ナノスケールのデバイスや医薬品を開発するための基盤になることが期待されます。

‘世界初！マイコプラズマの滑走運動における分子モーターの動きをナノレベルで検出！’. 大阪市立大学. https://www.osaka-cu.ac.jp/ja/news/2021/210528-2. (参照 2021-05-28.)

Kobayashi K, Kodera N, Kasai T, Tahara YO, Toyonaga T, Mizutani M, Fujiwara I, Ando T, Miyata M. 2021. Movements of Mycoplasma mobile gliding machinery detected by high-speed atomic force microscopy. mBio 12:e00040-21. https://doi.org/10.1128/mBio.00040-21.

補　足	■高速原子間力顕微鏡（高速 AFM） 　原子間力顕微鏡（Atomic Force Microscopy: AFM）は、探針と試料の間に働く原子間力を元に、分子の形状をナノメートル（10-9 m）程度の高い空間分解能で可視化する顕微鏡。高速 AFM は、金沢大学の安藤敏夫特任教授のグループによって開発された超高速で観察できる AFM で、サブ秒（～0.1 秒）という時間分解能で、水溶液中にあるタンパク質などの生体分子や細胞の形状や動態をその周囲の環境を含めて観察することができる。
参　考	動画：マイコプラズマ・モービレの滑走の様子 https://www.youtube.com/watch?v=-LRdogB3U8s

Kobayashi K, Kodera N, Kasai T, Tahara YO, Toyonaga T, Mizutani M, Fujiwara I, Ando T, Miyata M. 2021. Movements of Mycoplasma mobile gliding machinery detected by high-speed atomic force microscopy. mBio 12:e00040-21. https://doi.org/10.1128/mBio.00040-21.

AMERICAN SOCIETY FOR MICROBIOLOGY | mBio®

RESEARCH ARTICLE

Movements of *Mycoplasma mobile* Gliding Machinery Detected by High-Speed Atomic Force Microscopy

Kohei Kobayashi,[a] Noriyuki Kodera,[b] Taishi Kasai,[a]* Yuhei O. Tahara,[a,c] Takuma Toyonaga,[a] Masaki Mizutani,[a]* Ikuko Fujiwara,[a,d] Toshio Ando,[b] Makoto Miyata[a,c]

[a]Graduate School of Science, Osaka City University, Sumiyoshi-ku, Osaka, Japan
[b]Nano Life Science Institute (WPI-NanoLSI), Kanazawa University, Kanazawa, Ishikawa, Japan
[c]The OCU Advanced Research Institute for Natural Science and Technology (OCARINA), Osaka City University, Sumiyoshi-ku, Osaka, Japan
[d]Department of Bioengineering, Nagaoka University of Technology, Nagaoka, Niigata, Japan

Kohei Kobayashi and Noriyuki Kodera contributed equally to this work. Kohei Kobayashi performed most experiments and Noriyuki Kodera provided AFM setups and technologies.

ABSTRACT *Mycoplasma mobile*, a parasitic bacterium, glides on solid surfaces, such as animal cells and glass, by a special mechanism. This process is driven by the force generated through ATP hydrolysis on an internal structure. However, the spatial and temporal behaviors of the internal structures in living cells are unclear. In this study, we detected the movements of the internal structure by scanning cells immobilized on a glass substrate using high-speed atomic force microscopy (HS-AFM). By scanning the surface of a cell, we succeeded in visualizing particles, 2 nm in height and aligned mostly along the cell axis with a pitch of 31.5 nm, consistent with previously reported features based on electron microscopy. Movements of individual particles were then analyzed by HS-AFM. In the presence of sodium azide, the average speed of particle movements was reduced, suggesting that movement is linked to ATP hydrolysis. Partial inhibition of the reaction by sodium azide enabled us to analyze particle behavior in detail, showing that the particles move 9 nm right, relative to the gliding direction, and 2 nm into the cell interior in 330 ms and then return to their original position, based on ATP hydrolysis.

IMPORTANCE The *Mycoplasma* genus contains bacteria generally parasitic to animals and plants. Some *Mycoplasma* species form a protrusion at a pole, bind to solid surfaces, and glide by a special mechanism linked to their infection and survival. The special machinery for gliding can be divided into surface and internal structures that have evolved from rotary motors represented by ATP synthases. This study succeeded in visualizing the real-time movements of the internal structure by scanning from the outside of the cell using an innovative high-speed atomic force microscope and then analyzing their behaviors.

KEYWORDS AFM, probing, pathogenic bacteria, ATPase, class *Mollicutes*

Many bacteria translocate to nutrient-rich places and escape from repellent substances by manipulating external appendages, such as flagella and pili (1, 2). However, class *Mollicutes*, a small group of bacteria, have as many as three of their own motility mechanisms. Class *Mollicutes* evolved from phylum *Firmicutes* by losing peptidoglycan synthesis and flagella swimming to evade host innate immunity in their parasitic life (1). They have a single-layered cell membrane featured by a high content of sterols (25 to 30% of the weight of total membrane lipids) and lipoproteins as peripheral structures (3–7). Among *Mollicutes*, the gliding motility of *Mycoplasma mobile*, the subject of this study, is suggested to have evolved from a combination of ATP synthase and cell adhesion (1, 5, 8–12).

Citation Kobayashi K, Kodera N, Kasai T, Tahara YO, Toyonaga T, Mizutani M, Fujiwara I, Ando T, Miyata M. 2021. Movements of *Mycoplasma mobile* gliding machinery detected by high-speed atomic force microscopy. mBio 12: e00040-21. https://doi.org/10.1128/mBio.00040-21.

Editor Dominique Soldati-Favre, University of Geneva

Address correspondence to Makoto Miyata, miyata@sci.osaka-cu.ac.jp.

* Present address: Taishi Kasai, Department of Life Science, Rikkyo University, Toshima-ku, Tokyo, Japan; Masaki Mizutani, Bioproduction Research Institute, National Institute of Advanced Industrial Science and Technology (AIST), Tsukuba, Ibaraki, Japan.

Received 27 January 2021
Accepted 19 April 2021
Published 28 May 2021

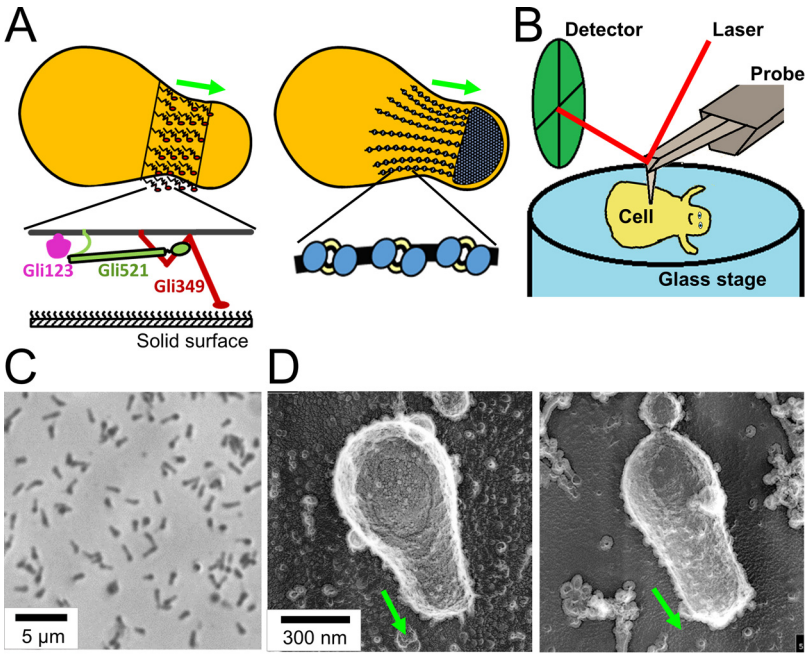

FIG 1 Experimental design and conditions for HS-AFM observation. (A) Schematic illustrations of *M. mobile* gliding machinery. The gliding machinery formed as a protrusion can be divided into surface (left) and internal (right) structures. The surface structure is composed of about 450 units, including three large proteins—Gli123 (purple), Gli521 (green), and Gli349 (red)—as shown at the bottom. Gli349 repeatedly catches sialylated oligosaccharides fixed on the solid surface and pulls the cell forward. The internal structure can be divided into a large mass at the cell front, "bell" and a chain structure. The chain structure is composed of particles that have been suggested to evolve from F-type ATPase/synthase. (B) Schematic illustration of an *M. mobile* cell being scanned by high-speed atomic force microscopy (HS-AFM). The surface of an immobilized cell on glass stage (blue) is scanned by an AFM cantilever probe (gray), and the cantilever movement is monitored by a detector (green). (C) Phase-contrast image of *M. mobile* cells on a coverslip. Living cells were immobilized onto a coverslip using poly-L-lysine and glutaraldehyde. (D) Quick-freeze, deep-etch electron microscopic (EM) image of *M. mobile* cells on a coverslip. The cell was immobilized on the coverslip by poly-L-lysine and glutaraldehyde (left) and allowed to glide on the coverslip coated with sialylated oligosaccharides (right). The cell axis and front are indicated by a green arrow in panels A and D.

M. mobile, isolated from a freshwater fish, is a flask-shaped bacterium with a length of 0.8 μm (Fig. 1A). *M. mobile* glides in the direction of its tapered end on solid surfaces, such as animal cells, glass, and plastics. Its gliding speed is 2.5 to 4 μm/s, which is 3 to 5 times its own cell length (10, 13). The gliding machinery is divided into surface and internal structures, both of which are composed of 450 units (Fig. 1A) (5, 8, 10, 14). The internal structure is characterized by multiple chains. An *M. mobile* cell has approximately 28 chains around the base of the protrusion (Fig. 1A). Each chain consists of uniformly sized particles, which are 13 nm in width and 21 nm in length (5). Interestingly, the amino acid sequence of component proteins suggests that this chain structure has evolved from ATP synthase (5, 8, 10, 12, 15). Recently, the isolated internal structure was shown to hydrolyze ATP through conformational changes, suggesting that the internal structure functions as a motor and generates the force for gliding (5, 10). The surface structure is composed of three large proteins, Gli349, Gli521, and Gli123. Gli349 has a binding site for sialylated oligosaccharide at its tip and plays the role of a "leg" in gliding (9, 16–20). Gli521 and Gli123 have been proposed to act as a "crank" that transmits force (21–24) and as a "mount" to correctly localize the surface proteins (19). A working model for the gliding mechanism has been suggested as follows (5, 10, 13, 25): the force for gliding generated based on ATP-derived energy by the special motor is transmitted across the membrane to the surface structure, including the leg structure. Then, the foot (the tip structure of the leg) repeatedly catches, pulls, and releases the sialylated oligosaccharides (9, 16), the major structures on host

animal surfaces (26–28), resulting in cell migration (21, 29–32). This explains the gliding mechanism at the bacterial surface; however, the spatial and temporal behaviors and movements of internal motors in living cells have not been examined.

Atomic force microscopy (AFM) (33) is a powerful method to image the surface structures and to study the mechanical properties of a biological sample at the submolecular level (34). In this method, a sample placed on a substrate is scanned with a nanometer-scale probe under dry and wet conditions. The usefulness of this method has been demonstrated also in the field of microbiology (35, 36). In high-speed AFM (HS-AFM), the scanning speed of AFM has been dramatically improved to ~20 frames per second (fps) while maintaining minimal invasiveness (37). Then, the dynamic behaviors of biomolecules and cells can be captured in aqueous solution (37), and their functional mechanisms have been elucidated (37–40). Notably, HS-AFM has been applied to understand the structures on the cell wall (41) or below the cell membrane (42).

In this study, we succeeded in visualizing the internal structure of *M. mobile* gliding machinery by scanning the surface of cells immobilized on a glass substrate using HS-AFM. The particle structure, a component of the internal structure, showed movements mainly in the right and inward directions relative to the gliding direction of an *M. mobile* cell.

RESULTS

Immobilization of living cells on the glass surface. We attempted to visualize the gliding machinery by scanning the upper side of living cells immobilized on the substrate surface (Fig. 1B), since the gliding machinery is arranged around the base of the protruded region (Fig. 1A). Cell suspension in a buffer was placed on a glass substrate reactivated for amino groups and kept for 10 min at 25 to 28°C. Phase-contrast microscopy showed that the cells adhered to the glass substrate at a density of 1 cell per approximately 6 μm^2 (Fig. 1C). When the buffer was replaced by growth medium containing sialylated oligosaccharides (scaffolds for gliding), half of the cells recovered to glide, suggesting that the cells were alive on the glass. Serum included in the medium contained sialylated oligosaccharides conjugated to fetuin, a serum protein. Fetuin was likely adsorbed onto the glass and worked as a scaffold for mycoplasma gliding (26–28, 43).

To observe the shape of immobilized cells, we adopted quick-freeze, deep-etch electron microscopy that visualizes cells under aqueous conditions with nanometer spatial resolution (44, 45). The morphology of immobilized cells (Fig. 1D, left) was not significantly different from that of the gliding cell visualized without any chemical fixation (Fig. 1D right).

Visualization of immobilized cells by HS-AFM. Next, the cells immobilized on the glass surface were scanned by HS-AFM (Movie S1 and Fig. 2A). A typical *M. mobile* cell with a flask shape was found at a density of a single cell per approximately 100 μm^2. As can be seen by comparing cell appearance in optical and electron microscopy, the cell images obtained here suggest that cells are characterized by rigidity in the front region (Fig. 1C and D), consistent with previous observations showing an internal rigid "bell" structure (5, 12). The average size of a cell was $0.93 \pm 0.33\ \mu m$ in length and $0.33 \pm 0.08\ \mu m$ in width ($n = 20$, Fig. 2A). We also measured the height along the long axis of the cell. Two peaks were found; one was near the front end, and the other was near the tail end of the cell, consistent with previously reported characteristics of *M. mobile* cells (49, 51).

The Young's modulus of the *M. mobile* cells was roughly estimated to be ~20 kPa based on the Hertz model of the spherical tip (46), by assuming that the Poisson's ratio of the cell and the nominal radius of the tip are 0.5 and ~5 nm, respectively. This value is comparable to that of live animal cells (10 to 100 kPa) (47), whose architecture of the cell membrane is a single lipid bilayer like *M. mobile* cells, but much smaller than that of live *Escherichia coli* cells (~8 MPa) (48), which have the outer membrane and the peptidoglycan layer.

To visualize the gliding machinery, the cell surface was scanned by HS-AFM at a

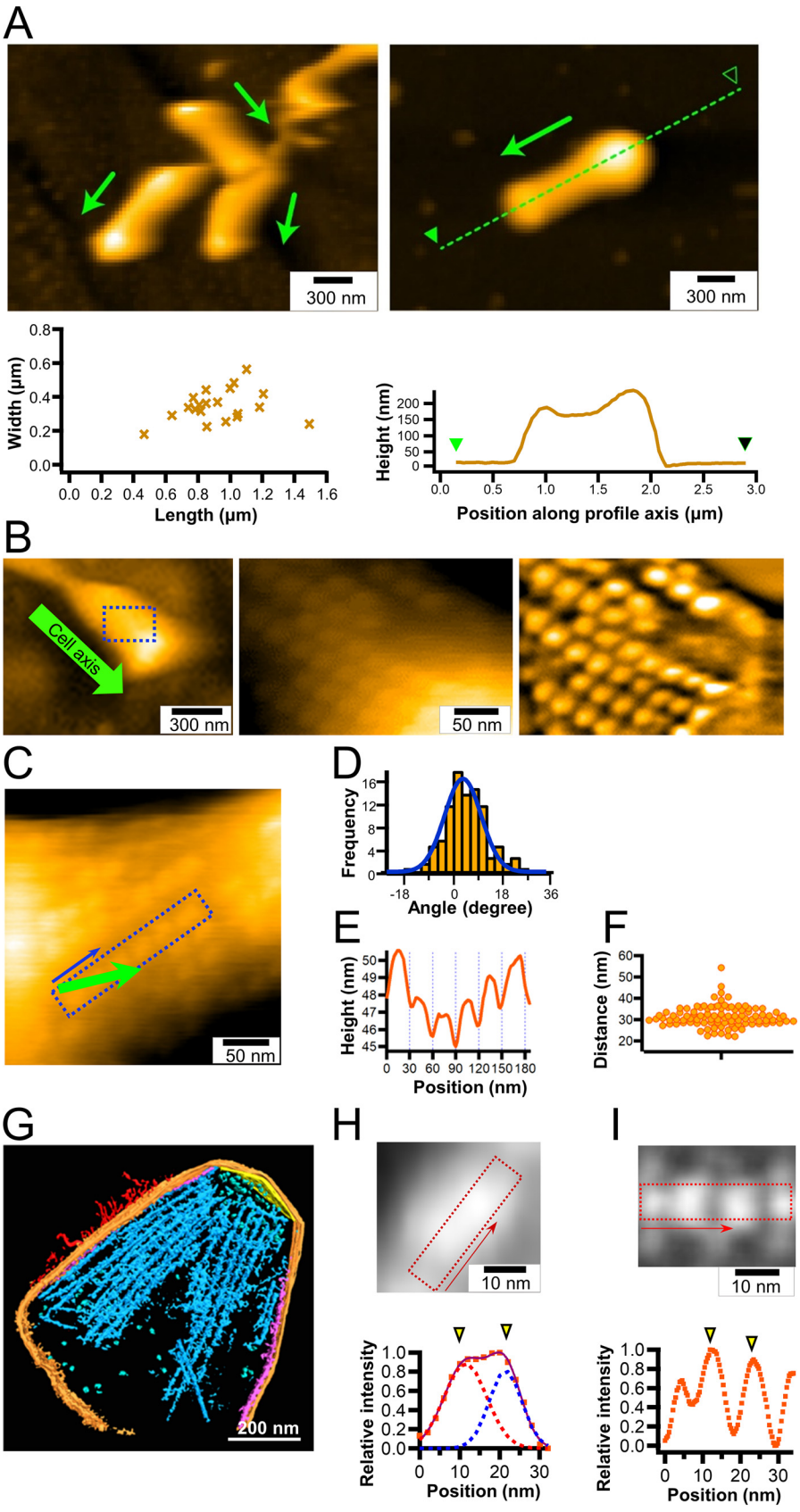

FIG 2 Chain imaging by HS-AFM. (A) (Left) Cluster of cells immobilized on a glass surface (upper) and distribution of cell dimensions ($n = 20$) (lower). (Right) The height profile along the broken line (upper)

(Continued on next page)

scanning rate of 300 ms per frame in an area of 300 nm^2. Interestingly, we found particle structures aligned mostly along the cell axis at the front side of the cells (Fig. 2B). The particle structures appeared when the average tapping force exceeded ~40 pN (piconewtons) (see Materials and Methods). They were aligned at an angle of approximately 4.6° relative to the cell axis (Fig. 2C and D, $n = 99$ chains from 20 cells). The particle height was approximately 2 nm (Fig. 2E), and the pitches were distributed as 31.5 ± 4.9 nm (Fig. 2F, $n = 98$), in good agreement with a previous number, 31 nm, measured by electron cryotomography (Fig. 2G) (5). To measure the dimensions of the particles in detail, we collected 19 particle images and averaged them (Fig. 2H). The averaged image showed an elliptical structure, 27.2 nm long and 14.2 nm wide, with two height peaks. The distance between the two peaks of a particle was 10.0 nm. These features were consistent with the results from electron cryotomography (Fig. 2I) (5), showing that the particle structure observed in HS-AFM is identical to the internal structure observed by electron cryotomography.

The internal structure of *M. mobile* is detected by HS-AFM from the surface. An *M. mobile* cell has three huge proteins, Gli521, Gli349, and Gli123, on its surface (Fig. 1A, left). To confirm that the particle structures visualized with HS-AFM are not the surface structures, the cell surface was treated with proteinase K, a serine protease with broad specificity, and scanned by HS-AFM. First, we confirmed that *M. mobile* cells gliding on the glass surface were stopped 1 min after the addition of 0.2 mg/ml proteinase K (Fig. S1A), suggesting that the surface proteins involved in the gliding machinery are sensitive to proteinase K. Then, we observed the cell surface by HS-AFM after the immobilized cells were treated with proteinase K for 20 min. The particle structures were observed on the surface of the cell even after proteinase K treatment. The particle pitches of cells with and without proteinase K treatment were 31.2 ± 3.2 ($n = 31$) and 28.9 ± 3.6 nm ($n = 33$), respectively (Fig. S1B), showing a significant difference between them ($P = 0.00651$ by Student's t test). Based on these observations, we concluded that the particle structure detected by HS-AFM was inside the structure but influenced by the surface treatment with proteinase K, consistent with a previous observation (12).

During the observation of intact cells immobilized on glass surfaces, we observed the removal of the cell membrane by chance, resulting in the exposure of the inside structure. The exposed inside structure showed features similar to the internal jellyfish-like structure of *M. mobile* (5, 12) (Movie S2, Fig. S1C). We compared the features of particle structures before and after the removal of the cell membrane (Fig. S1D). After removal, the height of the particle relative to the background increased, resulting in a clearer appearance than before removal. The particle pitches were 30.3 ± 4.1 and 31.8 ± 7.3 nm before and after removal, respectively, without a statistically significant difference ($P = 0.277$ by Student's t test). The average heights of particles observed before and after removal of the cell membrane were 257 and 18 nm, respectively, from the lowest position of the image. The difference between them was 239 nm, compara-

FIG 2 Legend (Continued)
is plotted along the green arrow (lower). The cell axis and front are shown by an arrow. (B) Detailed structure of a cell. (Left) Whole-cell image. The cell axis and front are indicated by a green arrow. (Middle) Magnified image of the boxed area of the left panel. (Right) The middle panel image was processed with a bandpass filter. (C to F) Image analyses of particles. (C) Cell image featuring a representative chain structure. The cell axis and front are indicated by a green arrow. (D) Distribution of chain angle relative to the cell axis fitted by a Gaussian curve ($n = 99$ chains from 20 cells). (E) Image profile of the boxed area along the direction of blue arrow in panel C. (F) Scatter dot plot for distances between peak positions of the chain profile. The average was 31.5 ± 4.9 nm ($n = 98$). (G) Three-dimensional rendered image for a 146-nm-thick slice of permeabilized cell reconstructed by electron cryotomography, modified from a previous study (5). The surface filamentous structures, cell membrane, undercoating at the front and side membranes, and internal chain are colored red, orange, yellow, and purple, respectively. (H) Averaged image of 19 particle structures from HS-AFM (upper) and image profile of boxed area (lower). The profile (orange squares) was fitted by the sum (purple solid line) of two Gaussian curves (red and blue). Yellow triangles show peaks of the Gaussian curves. (I) Averaged images of chain structure (blue part in panel G) from electron cryotomography (upper) (5) and image profile of the boxed area along the chain axis (lower). Yellow triangles show peaks of Gaussian curves. In all HS-AFM imaging, the surface was scanned left to right for line and lower to upper for image.

ble to the height of *M. mobile* cells (Fig. 2A and Fig. S1D). Therefore, the particles detected before and after cell membrane removal were proposed to be the structure beneath the upper cell membrane and the one on the lower cell membrane facing the glass substrate, respectively. This occasional observation is likely related to the character of *M. mobile* surface structure, that is a soft single-layered membrane (5). However, we could not remove the cell membrane intentionally. Then, we focused on analyzing the internal structure beneath the upper cell membrane.

Behavior of particle structure detected by HS-AFM. The surface protrusion of *M. mobile* cells was scanned with a scanning rate of 200 or 330 ms per frame with a scan area of 200 by 200 nm^2. Projected images were processed using a bandpass filter to improve the image contrast, by drift correction, and by averaging three sequential images for better signal/noise ratio (Movie S4). In most cases, the particles were difficult to trace over time because of image discontinuity, even when particle images were clear. This is probably due to the stability of the cell immobilized onto the glass surface and damage to the scanning probe. However, we succeeded in tracing the behaviors of individual particles in some videos and used them for further analyses.

Sodium azide suppressed particle movement. To discuss the behaviors of internal particles, we needed to confirm that the particle movements are caused by ATP hydrolysis on the internal structure. In a previous study, the ATPase activity of the internal structure of *M. mobile* was inhibited by sodium azide (5). The binding activity and gliding speed of "gliding heads," the gliding machinery isolated from the cell protrusion, were also inhibited by sodium azide (5). In the present study, we examined the effect of sodium azide on the gliding speed of intact *M. mobile* cells. The averaged gliding speed of intact *M. mobile* cells was decreased from 0.77 ± 0.17 to $0.04 \pm 0.02\,\mu$m/s by the addition of 15.4 mM sodium azide (Fig. 3A and B), suggesting that sodium azide affected the ATPase activity of the internal structure and the force generation for gliding.

We then scanned the cell surfaces by HS-AFM in the presence and absence of sodium azide (Movie S4 to S7). The tracking of the mass center every 200 ms (no azide) or 330 ms (with azide) for 16.2 s showed that most particles were moving independently (Fig. 3C). These movements were significantly reduced by the addition of sodium azide. We calculated the accumulated moving distances and estimated the speeds for the particle movements from a linear fitting of the accumulated moving distance (Fig. 3D and E). At concentrations of 0, 15.4, 76.5, and 765 mM sodium azide, the speeds calculated from accumulated moving distances were 6.9 ± 1.4, 3.9 ± 1.4, 3.6 ± 0.8, and 3.0 ± 1.1 nm/s, respectively, suggesting that the movement of particle structures is linked to ATP hydrolysis. Interestingly, in 15.4 mM sodium azide, the particles can be classified as either active or static, and the different types tend to form an adjacent pair in chains (Fig. 3C).

Particle displacements traced as an image profile. Not all particles moved in the same direction at the same time (Fig. 3C to E), and this feature was more obvious in 15.4 mM sodium azide (Movie S5, Fig. 4A), indicating that the movements were linked to ATP hydrolysis, not caused by artificial drift in the measurements. The addition of sodium azide may allow easier detection of individual movements by reducing some of the movements. Analysis of 27 particles in a 200 by 200 nm^2 field in the presence of 15.4 mM sodium azide for 23.1 s showed that 19 particles moved distances longer than 6 nm, distinct from other movements. The frequency of such long movements in the whole field was 1.17 events/s (Fig. 4A). Next, we focused on particle movements. Since the particles appeared to move mainly perpendicular to the particle chain in the cell surface plane, the height profile of a box perpendicular to the particle chain was traced over time (Fig. 4B, upper graphs). Six particles did not move (static particle), while 15 active particles showed remarkable movements, and a returning path for some particles was observed. As shown in the "a" panels of Fig. 4B and C, the movements of the particles showed a tendency moving 9.1 ± 2.5 nm ($n = 15$) in the left direction perpendicular to the chain axis and 2.3 ± 3.0 nm ($n = 8$) on the cytoplasmic side in the Z direction. These behaviors can be traced three-dimensionally as shown for the representative particle movements (Fig. 4B, lowermost graphs). The profile continued to change

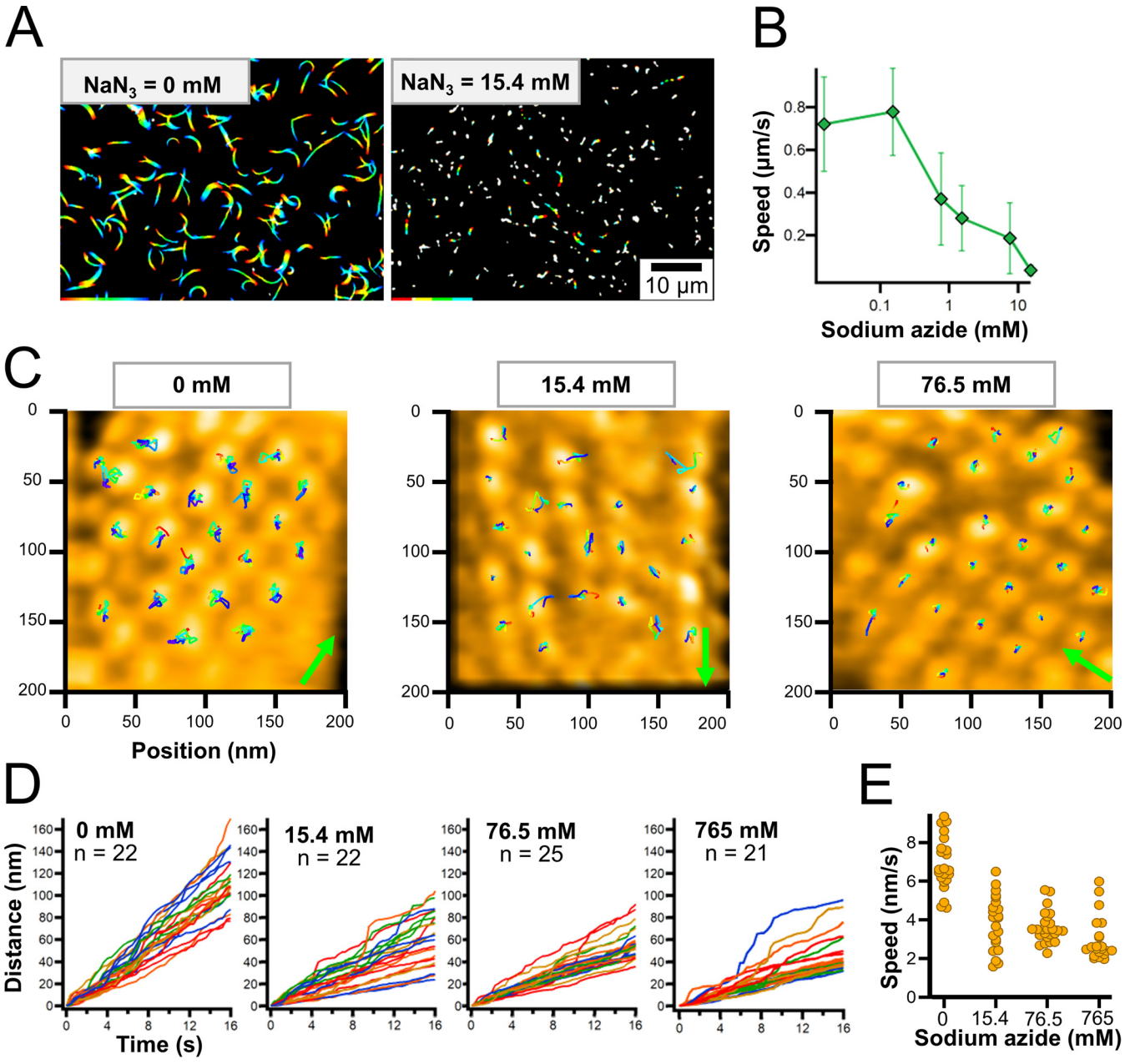

FIG 3 Effects of sodium azide on particle displacements. (A) Rainbow traces of gliding cells for 5 s with and without sodium azide from phase-contrast microscopy. Video frames were overlaid with different colors from red to blue. (B) Gliding speed under various concentrations of sodium azide. Speeds of 2.5 to 20 s were averaged for 140 to 223 cells. (C) HS-AFM images with continuous traces of individual particles for 13.2 s. HS-AFM images were processed by bandpass filter, drift correction, and sequential averaging. Particles were traced every 200 ms for no sodium azide, and 330 ms in the presence of sodium azide, as presented by the color change from red to blue. The cell axis and front are indicated by a green arrow. The surface was scanned left to right for line and lower to upper for imaging. Movies are shown as supplemental data as Movies S4, S5, S6, and S7 for imaging in 0, 15.4, 76.5, 765 mM sodium azide, respectively. (D) Time course of accumulated moving distances of individual particles under various concentrations of sodium azide. (E) Scatter dot plot of particle speed under various concentrations of sodium azide. Speeds were estimated from a linear fitting of accumulated moving distance.

for approximately five frames of 330 ms. However, the movement was likely completed in a single 330-ms frame, because the image was profiled after averaging three consecutive video images every 330 ms to reduce image noise. Eleven particles showed returning movements in the video, with speeds similar to those of their advancing movements, as shown in the panels marked "r" in Fig. 4B and C. In conclusion, the active particles moved to 9 nm left and 2 nm lower relative to the cell axis in 330 ms and came back to the original position in another 330 ms.

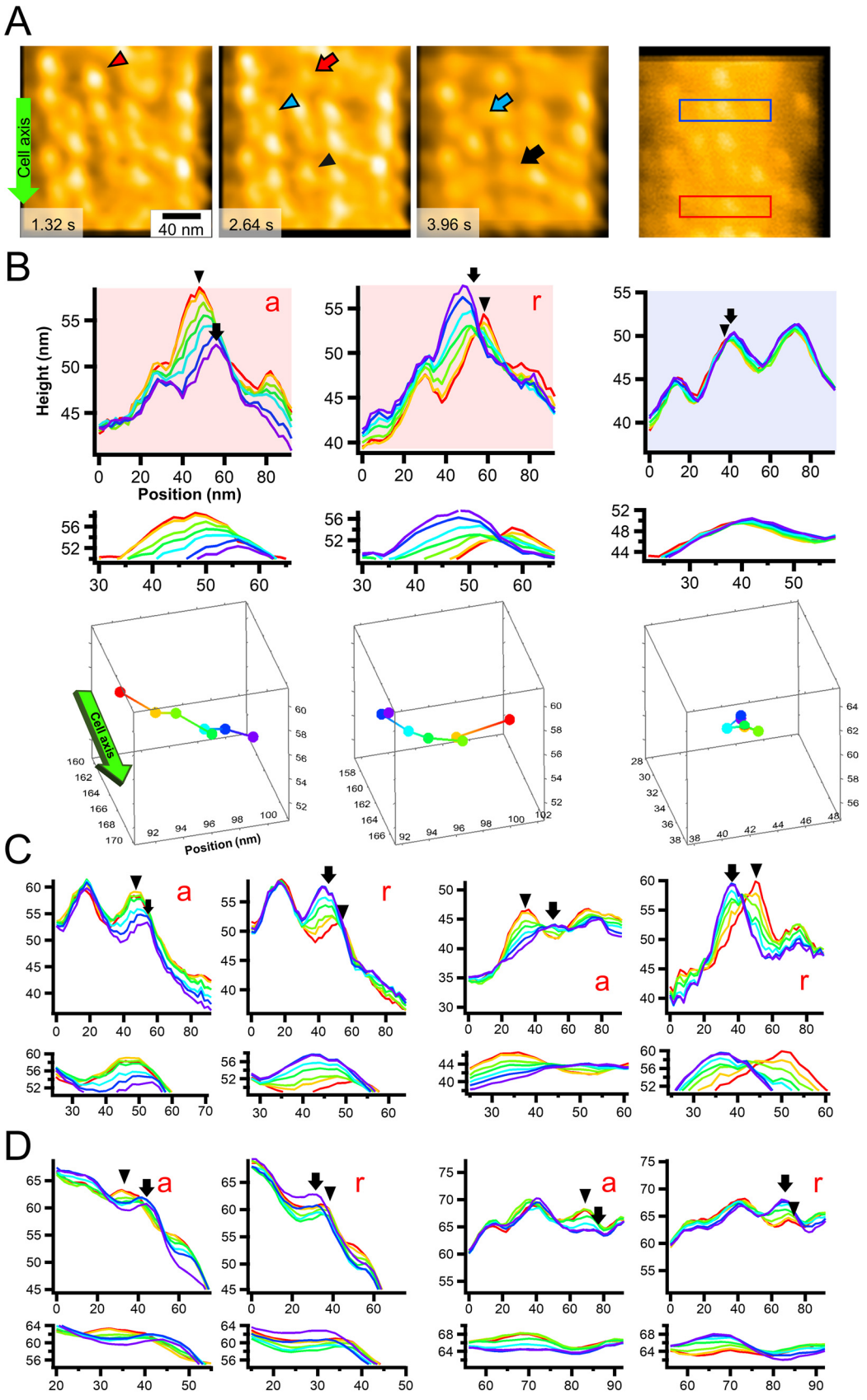

FIG 4 Movements of individual particles. (A) Video frames of particle chains under 15.4 mM sodium azide (Movie S5). The green arrow on the left shows the cell axis and front. The left three panels show consecutive video frames showing

(Continued on next page)

Next, particle movements perpendicular to the cell axis were searched in the absence of sodium azide. Observation of 21 particles for 16.6 s showed that movements longer than 6 nm appeared at a frequency of 2.17 events/s (Movie S4 and Fig. 4D). The distance moved was 8.0 ± 1.9 nm ($n = 24$) in the left direction perpendicular to the axis of the chain alignment within 200 ms and 2.0 ± 1.9 nm ($n = 18$) on the cytoplasmic side in the Z direction (Fig. 4D).

Particle displacements traced as a positional distribution. To study the direction of movements of the particles on the membrane surface statistically, the distributions of the particles as the mass center were analyzed every 200 and 330 ms for observations in the absence and presence of sodium azide, respectively (Fig. 5A and Movies S5 to S7). In this analysis, we determined the particle positions for the *x* and *y* axes (Fig. 5A), while only the *x* and *z* axes were shown in panels C and D of Fig. 4. Instead, we did not trace the particle positions with time in Fig. 5. The faster scan speed for the observation in the absence of sodium azide was applied, as we assumed that the particles moved faster under these conditions. However, this difference in the scanning speed should not affect the conclusion, because no difference was found, even when the analysis was performed using 400-ms intervals for the measurements without sodium azide (Fig. S2). Analysis showed that the distributions were larger in the presence of 15.4 mM and smaller at 76.5 and 765 mM than in the absence of sodium azide (Fig. 5A). Next, we measured the distributions of three distances (Fig. 5B) as follows: the particle position to the chain axis (Fig. 5C), the distance to the adjacent particle (Fig. 5D), and the distance to the adjacent particle projected to the chain axis (Fig. 5E). These results are schematically summarized (Fig. 5B), suggesting that movements perpendicular to the chain axis of the particles (presented as distance "c" in Fig. 5) should be present but not easy to detect in the absence of sodium azide; they were observed more clearly when the frequency of movements was reduced by sodium azide, and they were inhibited under high concentrations of sodium azide.

DISCUSSION

Internal structure was traced from the outside surface. The particle features traced by HS-AFM in this study were consistent with those of the internal structure reported in previous studies (Fig. 2) (5, 12), suggesting that HS-AFM visualized the internal structure. The large surface proteins Gli521, Gli349, and Gli123 exist on the cell surface of *M. mobile* as components of the gliding machinery (7, 14, 17–20, 22, 24, 49). A group of surface proteins, Mvsps, which are responsible for antigenic variations, also exist on the cell surface (3, 50). These surface proteins may interfere with probing the internal structure from the surface. However, the chain structures observed by HS-AFM did not show obvious differences before and after protease treatment of the cells (Fig. S1B). Furthermore, similar structures were observed before and after mechanical removal of the cell membrane (Fig. S1C and D). These results showed that the particles traced by HS-AFM were not on the surface structure, but were inside the cell. The surface structure, composed of mainly large filamentous proteins, may be too thin and/or mobile to be detected by the current scanning performance of HS-AFM on the cell

FIG 4 Legend (Continued)
remarkable particle movements. The particles with movements are marked before (triangles) and after (arrows) the movements with coordinated colors. Particles moved to the left relative to the gliding direction. The rightmost panel shows a raw image of the video frame showing areas profiled for active (red) and static (blue) particles shown in panel B. (B) Consecutive image profile of representative active and static particles. (Upper six graphs) Image profiles of active (red background) and static (blue background) particles every 330 ms for 1.98 s. (Lowermost graphs) Three-dimensional positions of peaks of particles tracing from red to purple. Y positions are shown only in these graphs in Fig. 4. The green arrow on the left shows the cell axis and front. (C) Consecutive image profiles showing particle movements every 330 ms for 1.98 s in 15.4 mM sodium azide. (D) Consecutive image profiles showing particle movements every 200 ms for 1.2 s without sodium azide (Movie S4). (B to D) Consecutive profiles of each frame from red to purple. Advancing (a) and returning (r) movements are presented. Peak positions of focusing particles are marked by a triangle and an arrow, respectively, for the initial and the end time points. Distances between peaks before and after movement were manually measured for statistical analysis of particle movements. The profile of heights and positions is presented with a common X- Y- scale in the lower panel for each data set.

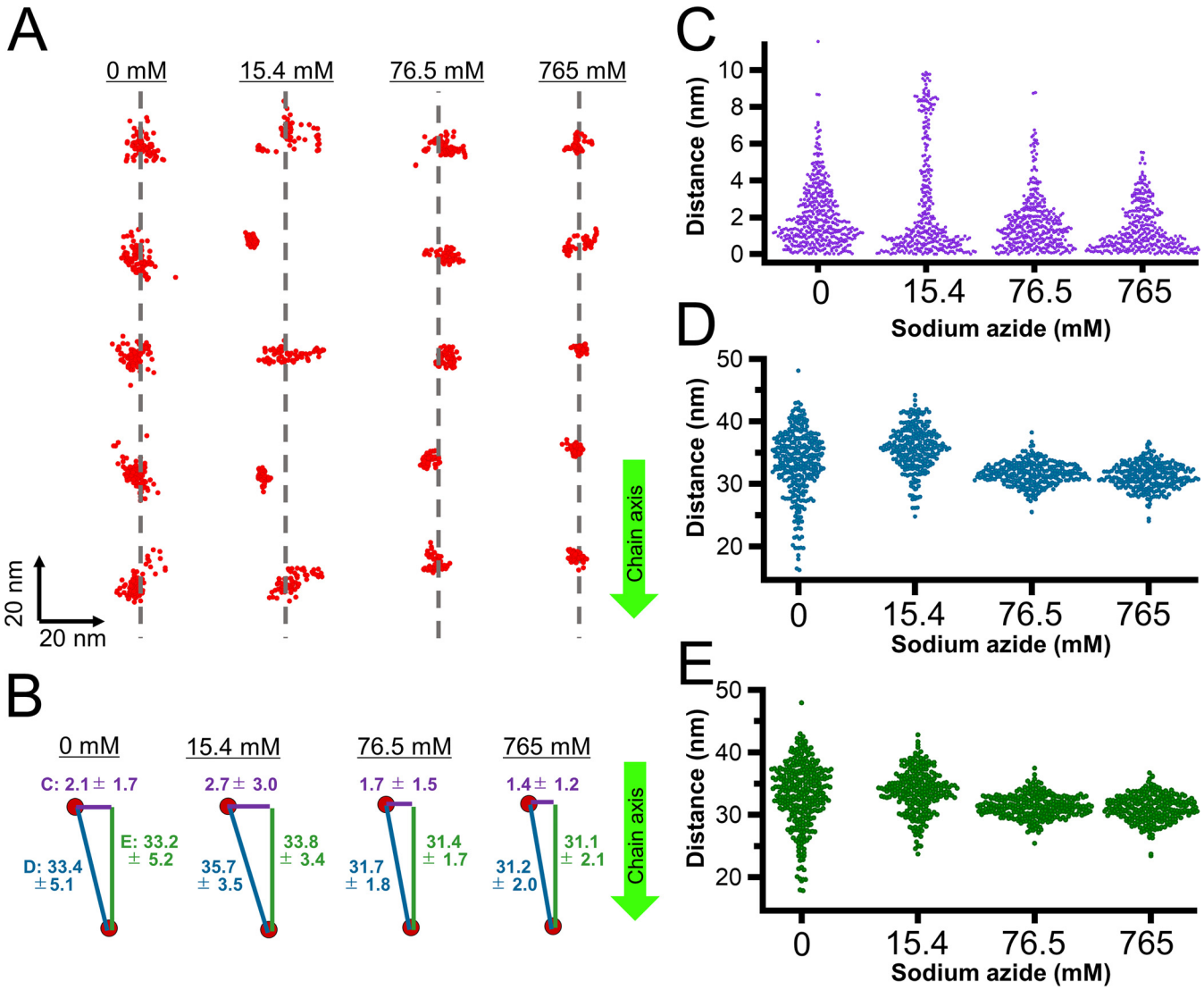

FIG 5 Analyses of particle distribution. (A) Distribution of particles in a chain. The particle positions and the axis of the particle positions are indicated by red dots and gray dashed lines, respectively. The particle positions were detected every 200 and 330 ms, respectively, without and with sodium azide at 82, 66, 70, and 66 points under 0, 15.4, 76.5, and 765 mM sodium azide, respectively. The axis of particle positions was determined by a linear approximation of the average position of each particle. (B) Schematic illustration of three distances with average and standard deviation (SD) values in nm. (C to E) The particle position to the chain axis (C, purple), the distance to the adjacent particle (D, blue), and the distance to the adjacent particle projected to the chain axis (E, green) are shown. Bar lengths are not to scale. Movies S4 to S7 were analyzed. The chain axis is indicated by a green arrow pointing mostly to the cell front in panels A and B.

membrane (16–18, 22). The lack of a peptidoglycan layer should be advantageous for visualizing the inside structure, due to the lack of stiffness (44, 45, 51). Moreover, the internal structure should be sufficiently stiff and positioned beneath the cell membrane, reminiscent of cortical actin in animal cells (42).

Effects of sodium azide. Sodium azide inhibits many ATPases by blocking ADP release (52). In *M. mobile* gliding, the reagent inhibited cell gliding (Fig. 3A and B) and the isolated gliding machinery (5). Particle behaviors became more visible in the presence of 15.4 mM sodium azide. Under this condition, cell gliding was reduced to 20 times slower than the original, suggesting that ATP hydrolysis occurred 20 times less frequently. If the particles move in a rapid and independent manner, it may be difficult to trace the movements of individual particles. However, if the reaction was partially inhibited by 15.4 mM sodium azide, most particles may be in their home position, while some particles move to another position. In this case, the movements could be traced easily. This assumption is supported by the observation that the particle

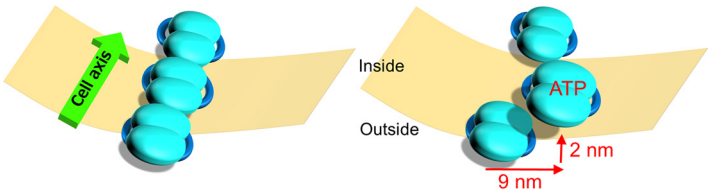

FIG 6 Schematic illustration of particle movement in *M. mobile* visualized by HS-AFM. The internal chain of the gliding machinery and cell membrane are indicated by blue objects and a beige plate, respectively. Here, we focus on the particle chain lining the lower side of cell membrane, while we scanned mostly the particle chain beneath the upper side of the cell membrane in this study. The left and right panels show the particles before and after the advancing movement, respectively. The central particle moves as an ATP- or ADP/P_i-bound form to the right and inner sides for a distance of 9 and 2 nm, respectively.

distances between neighboring particles are 1.7 to 2.5 nm shorter under high concentrations of sodium azide than those without the reagent (Fig. 5D). A previous study based on electron microscopy showed that the particle distances in the ADP and unbound forms were approximately 2 nm shorter than those in the AMPPNP, ADP-V_i, and ADP-AlF_x states (5). As sodium azide is thought to inhibit the release of ADP (52), the changes in particle distance observed in the present study are consistent with the results of electron microscopy (Fig. 5B) (5).

Particle behavior in the gliding mechanism. The particles moved approximately 9 nm to the right of the gliding direction and 2 nm to the cytoplasmic side within 330 ms (Fig. 6). This movement may be coupled with the transition from ADP or unbound form to ATP or the ADP/P_i form (5). Considering the fact that the particles are structurally linked to the surface structures of the gliding machinery (5), the movements observed in the present study are likely involved in the gliding mechanism.

There are two possibilities for the relation between the particle movements and gliding motility. As *M. mobile* gliding is caused probably by repetitive leg strokes (21, 29, 32), the particle movements may be coupled to the stroke. Previous studies have reported that the step size of *M. mobile* is approximately 70 nm under no load and adjustable to various loads (21, 29, 32, 53). The moving distances of particles, approximately 10 nm is much shorter than the step size. However, this difference can be explained because the surface structure contains two large proteins with dimensions comparable to the step size; that is, the Gli349 "leg" that catches the scaffold and the Gli521 "crank" that transmits force for gliding are 100 and 120 nm long, respectively (Fig. 1A) (16, 17, 22). Therefore, the movements occurring in the internal structure can be amplified through the huge protein molecules on the surface or through an unknown structure that connects the internal and surface structures (Fig. 1A and 2G). This assumption can explain the previous observation that the single leg exerts a force of 1.5 pN, a few times smaller than motor proteins (21), assuming elastic components are equipped in the large surface complex. Another possibility is that the movements observed here are caused as a "reaction" of cooperating many particles in a large complex, besides a direct transmission linking the particle and the surface structures. In this scenario, the movements of the transmission were too small to be detected by HS-AFM, for example rotation of rod proteins.

In a previous study, *M. mobile* gliding showed a leftward directional change of about 8.5° with 1-μm cell progress (31). This gliding property may be related to the observation that the particle movements are pointed to the right relative to the gliding direction (Fig. 6). Otherwise, the tilting of the chain axis about 4.6° from the cell axis may cause a directional change in gliding (Fig. 2D).

To elucidate the mechanism of *M. mobile* gliding, we need to further visualize the behaviors and structures of the machinery in detail, including those of both internal and surface structures. The combination of electron microscopy and HS-AFM may provide better insights in the near future.

MATERIALS AND METHODS

Cell preparation. A mutant strain (*gli521*[P476R]) of *M. mobile* 163K (ATCC 43663) activated for binding (21, 23, 54) was grown in Aluotto medium at 25 to 28°C, as previously described (8, 49). Cultured cells were collected by centrifugation at 12,000 × *g* for 4 min at 25 to 28°C and suspended in phosphate-buffered saline with glucose (PBS/G) consisting of 75 mM sodium phosphate (pH 7.3), 68 mM NaCl, and 10 mM glucose (21, 26, 30, 31). This process was repeated twice, and finally the cells were resuspended in PBS/G to a 20-fold density of the original culture.

Gliding analyses. A tunnel chamber assembled as previously described (3-mm interior width, 22-mm length, 40-μm wall thickness) was treated with Aluotto medium for 15 min at 25 to 28°C (21, 30), and then the medium was replaced by PBS/G. The cell suspension was inserted into the tunnel chamber with video recording. PBS/G was replaced with PBS/G containing 0.2 mg/ml proteinase K (Qiagen N. V., Hilden, Germany) or various concentrations of sodium azide, as necessary.

Cell immobilization on the glass surface. A glass slide was treated with saturated KOH-ethanol solution for 15 min and washed 10 times with water. For analyses with an imaging rate of 1,000 and 330 ms per frame, the glass was treated with 0.1% poly-L-lysine for 5 min. After the solution was removed, the glass was washed with water and dried. Then, the glass was treated with 0.1% glutaraldehyde for 5 min, washed with water, and covered with PBS/G. For analyses with an imaging rate of 200 ms per frame, the glass was treated with sandpaper, saturated with KOH-ethanol solution for 15 min, washed 10 times with water, and then dried. The washed glass was treated with 1,000-fold diluted 3-aminopropyldiethoxymethylsilane for 5 min at 25 to 28°C, washed, and treated with glutaraldehyde as described above. Finally, the cell suspension was placed onto the glass substrate and left for 10 min at 25 to 28°C.

Microscopy. To examine the immobilizing conditions using phase-contrast microscopy, the glass slide was assembled into a tunnel chamber (19). The cell suspension was loaded into the tunnel, kept for 10 min at 25 to 28°C, washed with PBS/G, and observed by phase-contrast microscopy IX71 (Olympus, Tokyo, Japan) (21, 27, 31). To analyze the immobilizing conditions, quick-freeze deep-etch electron microscopy, fixation, and washing were performed on the coverslip. When the cells were frozen without immobilization, we followed the procedure for the electron microscopy method described previously (44, 45). Briefly, the cells on the glass were pressed against a copper block cooled with liquid helium and frozen. Then, the frozen sample was fractured and etched to expose it. Subsequently, the exposed surface was shadowed with platinum to create a replica membrane, which was observed under a JEM-1010 transmission electron microscope (JEOL, Tokyo, Japan) at 80 kV, equipped with a FastScan-F214 (T) charge-coupled device (CCD) camera (TVIPS, Gauting, Germany).

Observation by HS-AFM. Imaging was performed with a laboratory-built HS-AFM in tapping mode (55, 56). Small cantilevers (BLAC10DS-A2; Olympus) with a resonant frequency of ~0.5 MHz in water, a quality factor (Q_c) of ~1.5 in water, and a spring constant (k_c) of ~0.08 N/m were used. The cantilever's free oscillation amplitude (A_0) and set-point amplitude (A_{sp}) were set at ~2.5 nm and ~0.8 × A_0, respectively. Under these conditions, the average tapping force $<F>$ can be approximated as ~40 pN using the following equation:

$$F = \frac{k_c}{2Q_c}\sqrt{A_0^2 - A_{sp}^2}$$

For searching cells, the sample was scanned at an imaging rate of 1,000 ms per frame in an area of 3,000 by 3,000 nm^2 with 150 by 150 pixels. To observe the particle structure, the cell surface was scanned with an imaging rate of 330 or 200 ms per frame in an area of 200 by 200 nm^2 with 100 by 100 pixels.

Video analyses. To trace particles in the XY plane, videos were processed by three methods (Movies S3 to S7). (i) The image contrast was improved by a bandpass filter. (ii) Image drifts were corrected by a plugin, "align slices in stack" (57), equipped with ImageJ. (iii) Image noises were removed by averaging three consecutive slices. Then, each particle image was cropped, binarized, and traced for the mass center. Here, the threshold for binarization was determined independently for each particle of interest. The cell axes in Fig. 2 were determined by fitting a cell image as an ellipse. All analyses were performed with ImageJ version 1.52A. Image averaging of particles was performed using EMAN, version 2.3.

SUPPLEMENTAL MATERIAL

Supplemental material is available online only.

MOVIE S1, AVI file, 0.2 MB.
MOVIE S2, AVI file, 2.7 MB.
MOVIE S3, AVI file, 2.6 MB.
MOVIE S4, AVI file, 0.8 MB.
MOVIE S5, AVI file, 0.6 MB.
MOVIE S6, AVI file, 0.7 MB.
MOVIE S7, AVI file, 0.6 MB.
FIG S1, PDF file, 0.3 MB.
FIG S2, PDF file, 0.2 MB.

ACKNOWLEDGMENTS

We appreciate Yuya Sasajima at Osaka City University for helpful discussions.

This work was supported by Grants-in-Aid for Scientific Research (A) (MEXT KAKENHI, grant number JP17H01544), JST CREST (grant number JPMJCR19S5), Osaka City University (OCU) Strategic Research Grant 2018 for top priority research, and by a Grant-in-Aid for the Fugaku Trust for Medicinal Research to M. Miyata.

REFERENCES

1. Miyata M, Robinson RC, Uyeda TQP, Fukumori Y, Fukushima SI, Haruta S, Homma M, Inaba K, Ito M, Kaito C, Kato K, Kenri T, Kinosita Y, Kojima S, Minamino T, Mori H, Nakamura S, Nakane D, Nakayama K, Nishiyama M, Shibata S, Shimabukuro K, Tamakoshi M, Taoka A, Tashiro Y, Tulum I, Wada H, Wakabayashi KI. 2020. Tree of motility: a proposed history of motility systems in the tree of life. Genes Cells 25:6–21. https://doi.org/10.1111/gtc.12737.
2. Nakamura S, Minamino T. 2019. Flagella-driven motility of bacteria. Biomolecules 9:279. https://doi.org/10.3390/biom9070279.
3. Adan-Kubo J, Yoshii SH, Kono H, Miyata M. 2012. Molecular structure of isolated Mvspl, a variable surface protein of the fish pathogen *Mycoplasma mobile*. J Bacteriol 194:3050–3057. https://doi.org/10.1128/JB.00208-12.
4. Kawamoto A, Matsuo L, Kato T, Yamamoto H, Namba K, Miyata M. 2016. Periodicity in attachment organelle revealed by electron cryotomography suggests conformational changes in gliding mechanism of *Mycoplasma pneumoniae*. mBio 7:e00243-16–e00216. https://doi.org/10.1128/mBio.00243-16.
5. Nishikawa M, Nakane D, Toyonaga T, Kawamoto A, Kato T, Namba K, Miyata M. 2019. Refined mechanism of *Mycoplasma mobile* gliding based on structure, ATPase activity, and sialic acid binding of machinery. mBio 10:e02846-19. https://doi.org/10.1128/mBio.02846-19.
6. Rottem S. 1980. Membrane lipids of mycoplasmas. Biochim Biophys Acta 604:65–90. https://doi.org/10.1016/0304-4157(80)90004-0.
7. Wu HN, Miyata M. 2012. Whole surface image of *Mycoplasma mobile*, suggested by protein identification and immunofluorescence microscopy. J Bacteriol 194:5848–5855. https://doi.org/10.1128/JB.00976-12.
8. Tulum I, Kimura K, Miyata M. 2020. Identification and sequence analyses of the gliding machinery proteins from *Mycoplasma mobile*. Sci Rep 10:3792. https://doi.org/10.1038/s41598-020-60535-z.
9. Hamaguchi T, Kawakami M, Furukawa H, Miyata M. 2019. Identification of novel protein domain for sialyloligosaccharide binding essential to *Mycoplasma mobile* gliding. FEMS Microbiol Lett 366:fnz016. https://doi.org/10.1093/femsle/fnz016.
10. Miyata M, Hamaguchi T. 2016. Prospects for the gliding mechanism of *Mycoplasma mobile*. Curr Opin Microbiol 29:15–21. https://doi.org/10.1016/j.mib.2015.08.010.
11. Tulum I, Yabe M, Uenoyama A, Miyata M. 2014. Localization of P42 and F_1-ATPase alpha-subunit homolog of the gliding machinery in *Mycoplasma mobile* revealed by newly developed gene manipulation and fluorescent protein tagging. J Bacteriol 196:1815–1824. https://doi.org/10.1128/JB.01418-13.
12. Nakane D, Miyata M. 2007. Cytoskeletal "jellyfish" structure of *Mycoplasma mobile*. Proc Natl Acad Sci U S A 104:19518–19523. https://doi.org/10.1073/pnas.0704280104.
13. Miyata M. 2010. Unique centipede mechanism of *Mycoplasma* gliding. Annu Rev Microbiol 64:519–537. https://doi.org/10.1146/annurev.micro.112408.134116.
14. Uenoyama A, Miyata M. 2005. Identification of a 123-kilodalton protein (Gli123) involved in machinery for gliding motility of *Mycoplasma mobile*. J Bacteriol 187:5578–5584. https://doi.org/10.1128/JB.187.16.5578-5584.2005.
15. Béven L, Charenton C, Dautant A, Bouyssou G, Labroussaa F, Skollermo A, Persson A, Blanchard A, Sirand-Pugnet P. 2012. Specific evolution of F_1-like ATPases in mycoplasmas. PLoS One 7:e38793. https://doi.org/10.1371/journal.pone.0038793.
16. Lesoil C, Nonaka T, Sekiguchi H, Osada T, Miyata M, Afrin R, Ikai A. 2010. Molecular shape and binding force of *Mycoplasma mobile*'s leg protein Gli349 revealed by an AFM study. Biochem Biophys Res Commun 391:1312–1317. https://doi.org/10.1016/j.bbrc.2009.12.023.
17. Adan-Kubo J, Uenoyama A, Arata T, Miyata M. 2006. Morphology of isolated Gli349, a leg protein responsible for *Mycoplasma mobile* gliding via glass binding, revealed by rotary shadowing electron microscopy. J Bacteriol 188:2821–2828. https://doi.org/10.1128/JB.188.8.2821-2828.2006.
18. Metsugi S, Uenoyama A, Adan-Kubo J, Miyata M, Yura K, Kono H, Go N. 2005. Sequence analysis of the gliding protein Gli349 in *Mycoplasma mobile*. Biophysics (Nagoya-Shi) 1:33–43. https://doi.org/10.2142/biophysics.1.33.
19. Uenoyama A, Kusumoto A, Miyata M. 2004. Identification of a 349-kilodalton protein (Gli349) responsible for cytadherence and glass binding during gliding of *Mycoplasma mobile*. J Bacteriol 186:1537–1545. https://doi.org/10.1128/jb.186.5.1537-1545.2004.
20. Kusumoto A, Seto S, Jaffe JD, Miyata M. 2004. Cell surface differentiation of *Mycoplasma mobile* visualized by surface protein localization. Microbiology (Reading) 150:4001–4008. https://doi.org/10.1099/mic.0.27436-0.
21. Mizutani M, Tulum I, Kinosita Y, Nishizaka T, Miyata M. 2018. Detailed analyses of stall force generation in *Mycoplasma mobile* gliding. Biophys J 114:1411–1419. https://doi.org/10.1016/j.bpj.2018.01.029.
22. Nonaka T, Adan-Kubo J, Miyata M. 2010. Triskelion structure of the Gli521 protein, involved in the gliding mechanism of *Mycoplasma mobile*. J Bacteriol 192:636–642. https://doi.org/10.1128/JB.01143-09.
23. Uenoyama A, Seto S, Nakane D, Miyata M. 2009. Regions on Gli349 and Gli521 protein molecules directly involved in movements of *Mycoplasma mobile* gliding machinery, suggested by use of inhibitory antibodies and mutants. J Bacteriol 191:1982–1985. https://doi.org/10.1128/JB.01012-08.
24. Seto S, Uenoyama A, Miyata M. 2005. Identification of a 521-kilodalton protein (Gli521) involved in force generation or force transmission for *Mycoplasma mobile* gliding. J Bacteriol 187:3502–3510. https://doi.org/10.1128/JB.187.10.3502-3510.2005.
25. Chen J, Neu J, Miyata M, Oster G. 2009. Motor-substrate interactions in *Mycoplasma* motility explains non-Arrhenius temperature dependence. Biophys J 97:2930–2938. https://doi.org/10.1016/j.bpj.2009.09.020.
26. Kasai T, Hamaguchi T, Miyata M. 2015. Gliding motility of *Mycoplasma mobile* on uniform oligosaccharides. J Bacteriol 197:2952–2957. https://doi.org/10.1128/JB.00335-15.
27. Kasai T, Nakane D, Ishida H, Ando H, Kiso M, Miyata M. 2013. Role of binding in *Mycoplasma mobile* and *Mycoplasma pneumoniae* gliding analyzed through inhibition by synthesized sialylated compounds. J Bacteriol 195:429–435. https://doi.org/10.1128/JB.01141-12.
28. Nagai R, Miyata M. 2006. Gliding motility of *Mycoplasma mobile* can occur by repeated binding to *N*-acetylneuraminyllactose (sialyllactose) fixed on solid surfaces. J Bacteriol 188:6469–6475. https://doi.org/10.1128/JB.00754-06.
29. Kinosita Y, Miyata M, Nishizaka T. 2018. Linear motor driven-rotary motion of a membrane-permeabilized ghost in *Mycoplasma mobile*. Sci Rep 8:11513. https://doi.org/10.1038/s41598-018-29875-9.
30. Tanaka A, Nakane D, Mizutani M, Nishizaka T, Miyata M. 2016. Directed binding of gliding bacterium, *Mycoplasma mobile*, shown by detachment force and bond lifetime. mBio 7:e00455-16. https://doi.org/10.1128/mBio.00455-16.
31. Morio H, Kasai T, Miyata M. 2016. Gliding direction of *Mycoplasma mobile*. J Bacteriol 198:283–290. https://doi.org/10.1128/JB.00499-15.
32. Kinosita Y, Nakane D, Sugawa M, Masaike T, Mizutani K, Miyata M, Nishizaka T. 2014. Unitary step of gliding machinery in *Mycoplasma mobile*. Proc Natl Acad Sci U S A 111:8601–8606. https://doi.org/10.1073/pnas.1310355111.
33. Binnig G, Quate CF, Gerber C. 1986. Atomic force microscope. Phys Rev Lett 56:930–933. https://doi.org/10.1103/PhysRevLett.56.930.
34. Muller DJ, Dufrene YF. 2008. Atomic force microscopy as a multifunctional molecular toolbox in nanobiotechnology. Nat Nanotechnol 3:261–269. doi:https://pubmed.ncbi.nlm.nih.gov/18654521/.
35. Dufrene YF, Viljoen A, Mignolet J, Mathelie-Guinlet M. 2021. AFM in cellular and molecular microbiology. Cell Microbiol 12:e13324. https://doi.org/10.1111/cmi.13324:e13324.
36. Pasquina-Lemonche L, Burns J, Turner RD, Kumar S, Tank R, Mullin N, Wilson JS, Chakrabarti B, Bullough PA, Foster SJ, Hobbs JK. 2020. The

architecture of the Gram-positive bacterial cell wall. Nature 582:294–297. https://doi.org/10.1038/s41586-020-2236-6.
37. Ando T. 2019. High-speed atomic force microscopy. Curr Opin Chem Biol 51:105–112. https://doi.org/10.1016/j.cbpa.2019.05.010.
38. Heath GR, Scheuring S. 2019. Advances in high-speed atomic force microscopy (HS-AFM) reveal dynamics of transmembrane channels and transporters. Curr Opin Struct Biol 57:93–102. https://doi.org/10.1016/j.sbi.2019.02.008.
39. Lyubchenko YL, Shlyakhtenko LS. 2016. Imaging of DNA and protein-DNA complexes with Atomic Force Microscopy. Crit Rev Eukaryot Gene Expr 26:63–96. https://doi.org/10.1615/CritRevEukaryotGeneExpr.v26.i1.70.
40. Rajendran A, Endo M, Sugiyama H. 2012. Structural and functional analysis of proteins by high-speed atomic force microscopy. Adv Protein Chem Struct Biol 87:5–55. https://doi.org/10.1016/B978-0-12-398312-1.00002-0.
41. Yamashita H, Taoka A, Uchihashi T, Asano T, Ando T, Fukumori Y. 2012. Single-molecule imaging on living bacterial cell surface by high-speed AFM. J Mol Biol 422:300–309. https://doi.org/10.1016/j.jmb.2012.05.018.
42. Zhang Y, Yoshida A, Sakai N, Uekusa Y, Kumeta M, Yoshimura SH. 2017. *In vivo* dynamics of the cortical actin network revealed by fast-scanning atomic force microscopy. Microscopy (Oxf) 66:272–282. https://doi.org/10.1093/jmicro/dfx015.
43. Jaffe JD, Miyata M, Berg HC. 2004. Energetics of gliding motility in *Mycoplasma mobile*. J Bacteriol 186:4254–4261. https://doi.org/10.1128/JB.186.13.4254-4261.2004.
44. Tulum I, Tahara Y, Miyata M. 2019. Peptidoglycan layer and disruption processes in *Bacillus subtilis* cells visualized using quick-freeze, deep-etch electron microscopy. Microscopy (Oxf) 68:441–449. https://doi.org/10.1093/jmicro/dfz033.
45. Miyata M, Petersen JD. 2004. Spike structure at the interface between gliding *Mycoplasma mobile* cells and glass surfaces visualized by rapid-freeze-and-fracture electron microscopy. J Bacteriol 186:4382–4386. https://doi.org/10.1128/JB.186.13.4382-4386.2004.
46. Lin DC, Dimitriadis EK, Horkay F. 2007. Robust strategies for automated AFM force curve analysis–I. Non-adhesive indentation of soft, inhomogeneous materials. J Biomech Eng 129:430–440. https://doi.org/10.1115/1.2720924.
47. Hecht FM, Rheinlaender J, Schierbaum N, Goldmann WH, Fabry B, Schaffer TE. 2015. Imaging viscoelastic properties of live cells by AFM: power-law rheology on the nanoscale. Soft Matter 11:4584–4591. https://doi.org/10.1039/c4sm02718c.
48. Mathelie-Guinlet M, Asmar AT, Collet JF, Dufrene YF. 2020. Lipoprotein Lpp regulates the mechanical properties of the *E. coli* cell envelope. Nat Commun 11:1789. https://doi.org/10.1038/s41467-020-15489-1.
49. Miyata M, Yamamoto H, Shimizu T, Uenoyama A, Citti C, Rosengarten R. 2000. Gliding mutants of *Mycoplasma mobile*: relationships between motility and cell morphology, cell adhesion and microcolony formation. Microbiology 146:1311–1320. https://doi.org/10.1099/00221287-146-6-1311.
50. Wu HN, Kawaguchi C, Nakane D, Miyata M. 2012. "Mycoplasmal antigen modulation," a novel surface variation suggested for a lipoprotein specifically localized on *Mycoplasma mobile*. Curr Microbiol 64:433–440. https://doi.org/10.1007/s00284-012-0090-y.
51. Nakane D, Miyata M. 2012. *Mycoplasma mobile* cells elongated by detergent and their pivoting movements in gliding. J Bacteriol 194:122–130. https://doi.org/10.1128/JB.05857-11.
52. Bowler MW, Montgomery MG, Leslie AG, Walker JE. 2006. How azide inhibits ATP hydrolysis by the F-ATPases. Proc Natl Acad Sci U S A 103:8646–8649. https://doi.org/10.1073/pnas.0602915103.
53. Miyata M, Ryu WS, Berg HC. 2002. Force and velocity of *Mycoplasma mobile* gliding. J Bacteriol 184:1827–1831. https://doi.org/10.1128/jb.184.7.1827-1831.2002.
54. Uenoyama A, Miyata M. 2005. Gliding ghosts of *Mycoplasma mobile*. Proc Natl Acad Sci U S A 102:12754–12758. https://doi.org/10.1073/pnas.0506114102.
55. Uchihashi T, Kodera N, Ando T. 2012. Guide to video recording of structure dynamics and dynamic processes of proteins by high-speed atomic force microscopy. Nat Protoc 7:1193–1206. https://doi.org/10.1038/nprot.2012.047.
56. Ando T, Kodera N, Takai E, Maruyama D, Saito K, Toda A. 2001. A high-speed atomic force microscope for studying biological macromolecules. Proc Natl Acad Sci U S A 98:12468–12472. https://doi.org/10.1073/pnas.211400898.
57. Tseng Q, Duchemin-Pelletier E, Deshiere A, Balland M, Guillou H, Filhol O, Thery M. 2012. Spatial organization of the extracellular matrix regulates cell-cell junction positioning. Proc Natl Acad Sci U S A 109:1506–1511. https://doi.org/10.1073/pnas.1106377109.